Please cite this article in press as: Robinson et al., Structural dynamics of dengue virus UTRs and their cyclization, Biophysical Journal (2025), https://doi.org/10.1016/j.bpj.2025.09.004

Biophysical Journal
Article

Biophysical Society

Structural dynamics of dengue virus UTRs and their cyclization

Zachary E. Robinson,[1] Higor Sette Pereira,[1] Michael H. D'Souza,[1] and Trushar R. Patel[1,2,3,*]
[1]Department of Chemistry and Biochemistry, Alberta RNA Research and Training Institute, University of Lethbridge, Lethbridge, Alberta, Canada; [2]Li Ka Shing Institute of Virology, University of Alberta, Edmonton, Alberta, Canada; and [3]Department of Microbiology, Immunology & Infectious Diseases, Cumming School of Medicine, University of Calgary, Alberta, Canada

ABSTRACT The dengue virus (DENV) poses a significant threat to human health, accounting for approximately 400 million infections each year. Its genome features a circular structure that facilitates replication through long-range RNA-RNA interactions, utilizing cyclization sequences located in the untranslated regions (UTRs). To gain new insights into the organization of the DENV genome, we purified the 5′ and 3′ UTRs of DENV in vitro and examined their structural and binding properties using various biophysical techniques combined with computational methods. Through our biophysical characterization, we determined the 5′ and 3′ UTR regions to bind with an affinity of 40 nM in a 1:1 stoichiometry. By using small-angle x-ray scattering, we provide the first structural characterization of the 3′ and 5′ UTR regions, revealing several plausible conformations that the viral UTRs may adopt during replication. This comprehensive investigation revealed key features that provide mechanistic insights into the different structural states during DENV replication, as tracked through the accessibility of various RNA conformations. Overall, our research enhances the understanding of DENV cyclization, emphasizing the structural adaptability, dynamic folding, and flexibility of these RNA molecules in solution. By uncovering details at the atomic level, we aim to contribute to the development of targeted drugs that can disrupt crucial stages of viral replication.

SIGNIFICANCE Our in vitro biophysical characterization demonstrated that the DENV UTRs interact in a 1:1 ratio with low binding affinity. By combining in-solution SAXS data with computational simulations, we emphasized the structural flexibility of DENV UTRs during replication. This study offers new insights into the organization of the DENV genome and highlights the adaptability of UTR structures, providing a fresh perspective on the virus's replication process.

INTRODUCTION

Flaviviridae viral family consists of more than 70 members and contains several highly infectious members such as dengue (DENV), Zika (ZIKV), and West Nile virus (WNV). This family of viruses is characterized by single-stranded, nonsegmented, positive-sense RNA genomes consisting of approximately 11,000 nucleotides and containing a unique open-reading frame that encodes three structural (C, E, prM) and seven nonstructural proteins (NS1, NS2A, NS2B, NS3, NS4A, NS4B, and NS5) (1). This genome is flanked by the highly structured 5′ and 3′ untranslated regions (UTRs) of RNA carrying a conserved short sequence at both ends. These conserved sequences of 11 nucleotides are known as the cyclization sequence (CS). The *Flavivirus* genome adopts a circular conformation (genome cyclization) through the basepairing of the 5′ and 3′ CSs, which is a crucial lifecycle phenomenon for viral replication to occur (2). DENV is one of the most infectious members of the *Flaviviridae* family, accounting for over 390 million infections a year (3). There are four main serotypes of DENV, which are present in their specific geographic locations (4). Of these serotypes, dengue serotype 2 (DENV2) has the greatest societal impact and is responsible for the largest number of cases and severe outcomes upon infection (5–7). The genomes of all four DENV serotypes essentially contain two major sequence components that regulate genome cyclization, composed of the 5′ and 3′ CSs along with the upstream AUG regions (UARs) (8,9). Both regulatory sequences are present in the 3′ UTR of the viral genome, whereas the 5′ CS is found downstream of the 5′ UTR in a

Submitted May 6, 2025, and accepted for publication September 2, 2025.

*Correspondence: trushar.patel@uleth.ca

Zachary E. Robinson and Higor Sette Pereira contributed equally to this work.

Editor: Frank Gabel.

https://doi.org/10.1016/j.bpj.2025.09.004

Please cite this article in press as: Robinson et al., Structural dynamics of dengue virus UTRs and their cyclization, Biophysical Journal (2025), https://doi.org/10.1016/j.bpj.2025.09.004

part of the sequence that codes for the viral capsid protein (10).

Vaccine development efforts against DENV have persistently faced challenges due to cross-reactivity with other flaviviruses, such as the ZIKV (10). Although recent efforts have uncovered two promising candidates, some skepticism remains regarding the safety of the vaccines (11,12). The safety of dengue vaccines is paramount, especially since some vaccines have been associated with an increased risk of severe dengue in certain populations, particularly among those who have not been previously infected with the virus (12). Additionally, there are logistical concerns regarding the feasibility of distributing newly developed vaccines, particularly due to geographical limitations in vaccine storage and distribution, as well as geopolitical instability in developing nations most affected by mosquito reservoirs (13). Although there are currently no potential therapeutic options on the market, an increased understanding of DENV viral replication would undoubtedly support the identification of novel therapeutic targets. For this reason, DENV replication has been well characterized, and multiple studies have investigated the functional and biological significance of DENV cyclization during the viral life cycle (8,9). A previous study found highly structured and conserved regions with low mutation rates in different DENV and ZIKV strains (14). Despite sequence differences, the study also revealed preserved interactions across serotypes, suggesting that longer-range interactions are essential for viral fitness. However, a comprehensive study of the high-resolution structural characterization of this long-range RNA-RNA interaction remains elusive.

In this study, we performed a comprehensive analysis of the structure of DENV UTRs using both computational and biophysical approaches. We synthesized and purified both UTRs in vitro and identified the RNA-RNA complexes via size-exclusion chromatography combined with multiangle light scattering (SEC-MALS). To better understand the structural envelope of the DENV UTRs, both individually and as a complex, we employed small-angle x-ray scattering (SAXS). We then developed coarse-grained computational models of the RNAs using SimRNA, incorporating secondary structure constraints from previously established chemical probing techniques. These models were aligned with the SAXS envelopes, revealing the dynamic and flexible nature of the DENV 5′ and 3′ structures. Additionally, we refined the coarse-grained models to fit within their respective SAXS envelopes using MDfit-GROMACS, generating optimized all-atom, structure-based models with improved congruence under SAXS electron density map constraints. Characterizing these structures could form a basis for potential antiviral treatments aimed at blocking viral replication by preventing cyclization and may also enhance understanding of DENV replication mechanisms.

MATERIALS AND METHODS

Plasmid constructs

The full genome sequence of serotype 2 DENV was obtained from the NCBI database (NCBI: NC_001474) (15). The noncoding terminal regions of the virus were identified using the annotated genome and inserted into separate pUC57 vectors (IDT, Canada) as previously described (16–18). The sequence properties of the UTRs are listed in Table S1. Briefly, vectors containing both the 5′ and 3′ UTRs were created, along with a construct that included part of the 5′ translated region to ensure the presence of the CS. Mutants were designed with the assistance of the IntaRNA 2.0 tool (19). The mutant construct was prepared by modifying specific sequence elements integral for DENV genome cyclization, resulting in disruption to the noncoding terminal region complementarity.

Synthesis and purification of DENV 5′ and 3′ UTR RNA

The RNA was synthesized by runoff in vitro transcription using an in-house purified T7 polymerase as described (18). Briefly, a linearized plasmid containing the DNA sequence of the RNA was incubated in a reaction mixture for 4 h at 37°C. Due to their size, the DENV 3′ constructs were digested with 40 U of DNase (New England Biosciences, MA) for 1 h at 37°C before RNA purification. All RNA samples were purified using a Superdex 200 Increase GL 10/300 (Global Life Science Solutions USA, Marlborough, MA, USA) coupled with an ÄKTA Prime Pure FPLC (Cytiva, USA). RNA was eluted using the RNA buffer (10 mM Bis-Tris pH 5.5, 100 mM NaCl, 10 mM KCl, 5 mM $MgCl_2$, and 5% glycerol) at a flow rate of 0.5 mL/min. RNA samples were analyzed on a 2% agarose gel at 100 V for 35 min to assess quality, and their concentration was determined by measuring absorbance at 260 nm using a Biodrop (MBI Lab Equipment).

DENV 5′ and 3′ UTR RNA labeling

RNA samples were labeled as described previously (18). Briefly, purified RNA samples were concentrated to approximately 100 μM through ethanol precipitation. One milligram of Alexa Fluor 488 dye (Thermo Fisher, CA) was resuspended in 175 μL of DMSO. A labeling reaction was prepared using 30 μL of concentrated RNA, 1.25 mg of 1-ethyl-3-(3-dimethylamino) propyl carbodiimide hydrochloride, and 10 μL of the dye solution. The samples were pipetted until the contents were dissolved, and then 20 μL of 0.1 M imidazole (pH 6.0) was added. The samples were incubated at room temperature for 3 h before being passed over a Superdex 200 10/300 GL column. RNA was checked for degradation using native agarose gel electrophoresis and for labeling efficiency using NanoTemper Technologies Monolith NT.115 microscale thermophoresis (MST) by quantifying fluorescence counts.

Microscale thermophoresis

All microscale thermophoresis interaction studies were performed after labeling the 3′ UTR. In each case, a two-fold serial dilution was performed on the 5′ UTR from a starting concentration of ∼20 μM. Then, labeled 3′ UTR was added to a final concentration of 81 nM. Mixtures were incubated at 37°C for 3 h and then analyzed as previously described (18). Briefly, samples were loaded into a NanoTemper Technologies Monolith NT.115 (Munich, Germany) using standard capillaries. Thermophoresis was measured at room temperature (22°C) and performed with 90% excitation power and medium IR laser power. Initial fluorescence migration was measured from −1.0 to 0.0 s and used to normalize the measured fluorescent migration time (9.0–10.0 s). Three independent replicates were analyzed using MO.Affinity Analysis software v2.1.3 and fit to the standard K_D fit model, which describes a 1:1 stoichiometric molecular interaction according to the law of mass action (20).

Please cite this article in press as: Robinson et al., Structural dynamics of dengue virus UTRs and their cyclization, Biophysical Journal (2025), https://doi.org/10.1016/j.bpj.2025.09.004

Multiangle light scattering

Multiangle light scattering was performed using Dawn and Optilab instruments, as previously described (18). Samples were concentrated and loaded onto a Vanquish autosampler in 100-μL increments. Samples were then run through a Shodex KW403-4F SEC column (Showa Denko America, New York, NY, USA) at a flow rate of 0.16 mL/min using a Thermo Scientific Vanquish Core HPLC System (Thermo Fisher, CA). Data collection was performed at 20°C. All samples were measured in RNA buffer. The 5′ UTR, 3′ UTR, and complex samples were measured using a dn/dc of 0.172. Data were analyzed using Astra v8.0.0.25, and absolute molecular weight (*M*w) was calculated using Eq. 1 for each elution point, where: *R* (θ) is Rayleigh's ratio, *K* is the polymer constant, and *c* is the concentration of the solution.

$$M_w = \frac{R(\theta)}{K * c} \tag{1}$$

Small-angle x-ray scattering

As previously reported (21), SAXS data collection was performed on the B21 HPLC-SAXS beamline at Diamond Light Source (Didcot, Oxfordshire, UK). An Agilent 1200 (Agilent Technologies, Stockport, UK) HPLC was utilized through connection to a specialized flow cell. A Shodex 403KW-4F column was equilibrated with RNA buffer, and 50 μL of purified sample was injected with a flow rate of 0.160 mL/min. Sample concentration was determined using a Biodrop, and the data were collected using 1.0 mg/mL of 5′, 0.7 mg/mL of 3′, and a 1:1 mixture containing 0.7 mg/mL of 5′ and 3′. Frames were exposed to synchrotron radiation (x-rays) for 3.0 s for a total of ∼600 frames. The resulting data were buffer-subtracted using automated Chromixs selection for each sample peak, and then data analysis was performed using the ATSAS suite of programs (22,23). The radius of gyration (R_g) and sample quality were evaluated through Guinier analysis (24). The relative folding quality of each RNA molecule was determined through dimensionless Kratky analysis (25). GNOM was used to perform paired distance distribution $P(r)$ analysis to obtain real-space R_g and maximum particle dimension (D_{max}) measurements (26,27). Using the $P(r)$ derived information, 20 models were generated for the 5′ UTR and 100 models for the 3′ UTR using DAMMIN (28) on slow mode with a maximum of 200 annealing steps. A larger number of models was generated for the 3′ UTR due to its larger size, as previously shown to be necessary (18), whereas 20 models proved to converge to a single output for the 5′ UTR. After DAMMIN, 5′ UTR models were averaged and filtered to produce a single representative model using DAMAVER and DAMFILT (28,29). Due to the large size of the 3′ UTR, we decided to cluster representative models instead of generating a singular averaged model via DAMCLUST (29), and merging clusters with discrepancies inferior to 0.05 normalized spatial discrepancy (NSD) units.

Determination of RNA's tertiary structures

To determine the RNA's tertiary structure, we retrieved experimental secondary structure information from previously published chemical probing techniques on the DENV 5′ and 3′ UTRs (14). These secondary structure constraints, in the form of a dot-bracket profile, were then used in SimRNA v3.20 (30) for generating three-dimensional, coarse-grained models. SimRNA is a software tool that utilizes a coarse-grained model for RNA structure and operates as a Monte Carlo sampler. To simulate the 5′-3′ UTR cyclization complexes, the secondary structure information of the 5′ and 3′ UTRs was maintained, including all their central structural units. At the same time, modifications were applied to each end to enable basepairing of the CS and UAR. For the analysis of the DENV UTRs, we performed 20 million SimRNA iterations in replica exchange mode. Subsequently, we carried out SimRNA clustering within the lowest 1% of all trajectories based on energy. The SAXS DAMFILT or DAMCLUST structures were used to fit the representative tertiary structures that were computationally generated, which consisted of 2000 high-resolution models. The fitting process was performed using DAMSUP for all studied conditions (5′ UTR, 3′ UTR, and 5′-3′ complex) (31). Further selection was conducted to represent the atomistic RNA model. The chosen models exhibited an NSD value of 0.90–1.4, indicating a close fit between the low-resolution electron density envelopes and their associated coarse-grained models (32). Using UCSF ChimeraX 1.8, we superimposed the SAXS models with their respective high-fitting tertiary structure, coarse-grained models to better evaluate visual fitting through "Fit-in-Map" and correlative fit by correlation coefficient (33).

All-atom, structure-based molecular dynamics simulations of RNA's tertiary structures

We performed all-atom structure-based molecular dynamics (MD) simulations using MDfit-GROMACS to enhance the alignment of the previously determined secondary structures of the viral noncoding terminal region RNAs with the newly identified DENV UTR SAXS envelopes (34,35). We generated PDB structures of representative coarse-grained SimRNA models that showed high fitting values and overlap with the SAXS envelopes of the RNAs. Utilizing the web service SMOG (Structure-based Models for Biomolecules), we created topology files that included force field parameters for modeling the representative PDBs (36,37). All nonbonded contacts in the initial structures were defined using a cutoff distance of 4.5 Å. Simulations for each RNA were performed using the following potential:

$$V = V^{SB} + V^{map} = V^{SB} - W\sum_{ijk}\rho_{ijk}^{sim}\rho_{ijk}^{exp} \tag{2}$$

Here, V^{SB} is the potential of the structure-based simulation, W is the energetic weight of the map (the weights, or atomic numbers, considered for the three molecules were 3752 for 5′ UTR, 9332 for 3′ UTR, and 13,084 for the 5′-3′ complex), and ρ_{ijk}^{sim} and ρ_{ijk}^{exp} are the normalized simulated and experimental densities at voxel (i,j,k) corresponding to the model and the SAXS envelope (38). V^{SB} is further described with the following equations:

$$\begin{aligned} V^{SB} = & \sum_{bonds}\frac{\varepsilon_r}{2}(r_i - r_{i,o})^2 + \sum_{angles}\frac{\varepsilon_\theta}{2}(\theta_i - \theta_{i,o})^2 \\ & + \sum_{impropers}\frac{\varepsilon_{\chi i}}{2}(\chi_i - \chi_{i,o})^2 + \sum_{planar}\frac{\varepsilon_{\chi p}}{2}(\chi_i - \chi_{i,o})^2 \\ & + \sum_{backbone}\varepsilon_{BB}F_D(\phi_i - \phi_{i,o}) \\ & + \sum_{sidechains}\varepsilon_{SC}F_D(\phi_i - \phi_{i,o}) \\ & + \sum_{contacts}\epsilon_C\left[\left(\frac{\sigma_{ij}}{r_{ij}}\right)^{12} - 2\left(\frac{\sigma_{ij}}{r_{ij}}\right)^{6}\right] \\ & + \sum_{non-contacts}\varepsilon_{NC}\left(\frac{\sigma_{NC}}{r_{ij}}\right)^{12} \end{aligned} \tag{3}$$

It is further incorporated by the dihedral potential, $\varepsilon F_D(\phi)$:

$$\varepsilon F_D(\phi) = \varepsilon(1 - cos\phi) + \frac{\varepsilon}{2}(1 - cos\,3\phi), \tag{4}$$

Please cite this article in press as: Robinson et al., Structural dynamics of dengue virus UTRs and their cyclization, Biophysical Journal (2025), https://doi.org/10.1016/j.bpj.2025.09.004

with variables defined as $\varepsilon_r = 50\ \varepsilon_0$, $\varepsilon_\theta = 40\ \varepsilon_0$, $\varepsilon_{\chi i} = 10\ \varepsilon_0$, $\varepsilon_{\chi p} = 40\ \varepsilon_0$, $\varepsilon_{NC} = 0.1\ \varepsilon_0$, $\sigma_{NC} = 2.5$ Å, and $\varepsilon_0 = 1$.

To calculate a simulated map, each atom in the model was represented by a Gaussian function with a width of 5.0 Å and a truncated tail at 1% of the peak value. The SAXS-filtered PDB files, representing the definitive models of the large RNA clusters, were converted into mrc-formatted maps using ChimeraX version 1.8 and subsequently transformed into sit files with Situs (33,39). The SAXS envelopes provided a spatial constraint for the all-atom models to undergo folding while adjusting atom-to-atom distances, bond lengths, and bond angles. MDfit, compiled with FFTW, was used to enable the RNAs to fit within the SAXS envelope. We utilized the MDfit-modified version of GROMACS (version 4.5.5) to perform MD simulations (40–42). The simulations were conducted for 200,000 iterations with a timestep of 0.002 in reduced units (40–42).

RESULTS AND DISCUSSION

DENV2 UTRs are homogeneous and bind at the low nanomolar range

To obtain DENV2 5′ and 3′ UTR RNAs, we performed in vitro transcription and purified the synthesized RNA using SEC. DENV2 UTRs were successfully purified, eluting in a typical Gaussian profile with 3′ UTR capping absorbance detectors from 8.5 to 11.5 mL. In comparison, the 5′ UTR eluted from 12.0 to 14.0 mL (Fig. S1). An RNA of similar size to the 178 nucleotides of the 5′ UTR was observed eluting at approximately 11 mL by Kim et al., suggesting that the observed elution volumes fall within the reasonable range for RNAs of that size (43). Sample quality was assessed using agarose gel electrophoresis (Fig. S1, inset), which showed homogeneous and monomeric RNA. An additional set of mutant RNAs was transcribed and purified in a similar manner (Fig. S1 *C*). Minimal changes in behavior were observed in SEC or nondenaturing gels for this RNA (Fig. S1, inset).

Next, we employed SEC-MALS to further confirm the quality of the transcribed RNAs, determine their molecular weights (M_w), and assess their homogeneity in solution. This technique holds significant value for the biophysical characterization of RNA molecules in solution (44–46). Values of 57.93 ± 3.1 kDa and 161.20 ± 2.7 kDa were calculated from the scattering data for the 5′ and 3′ UTRs, respectively (Fig. 1 *A* and *B*). These values align well with the expected molecular weights (M_w) for the RNAs, as calculated from their theoretical sequences (57.4 kDa and 159.6 kDa, respectively). This indicates that the UTR RNAs were monomeric and exhibited minimal to nondetectable degradation or oligomerization, confirming that monodisperse monomeric molecules were used for all subsequent studies. Upon confirming the homogeneity of the sample, we investigated the RNA-RNA interaction between the 5′ and 3′ UTRs. We demonstrated that the absolute molecular weight of the complex is 209.0 ± 19.0 kDa (Fig. 1 *C*). This value falls within an error range of the expected value (217.0 kDa) for a 1:1 stoichiometric ratio of the 5′ and 3′ UTR in the complex. A 1:1 ratio is expected due to the 5′-3′ UTR interaction and its role in cyclizing the genome for replication (8,9,47). To the best of our knowledge, this is the first experiment demonstrating that the interaction between the DENV 5′ and 3′ UTRs follows a 1:1 stoichiometry. This result also aligns with recent work on the cyclization of the Japanese encephalitis virus (JEV) genome, showing that this RNA-RNA interaction upholds a 1:1 interaction stoichiometry in vitro (18).

Subsequently, the binding affinity between DENV UTRs was determined using MST. Although the affinity of the cyclization interaction has previously been determined to be 8 nM by electrophoretic mobility shift assay, this binding affinity has not yet been described with an orthogonal and more robust method (9). MST has been identified as an ideal method for quantifying and measuring RNA-RNA interactions and was previously used to characterize the binding affinity of the JEV cyclization interaction (18,20). We demonstrated that the K_D value for the interaction between the terminal regions of DENV is approximately 40 nM (Fig. 1 *D*). This aligns with previously reported values for the viral family as the cyclization of the JEV terminal regions were shown to have a K_D of 60 nM, whereas the cyclization of WNV was determined to have a K_D value of 32 nM (18,48). Our experiments align well with these values, as well as with previous work on the dengue viral terminal regions, where a K_D value of 8 nM was identified (9,49). Additionally, we conducted a study to determine if the binding identified was exclusively linked to the CS or if other sequences and structural elements were involved. We designed a mutant of the DENV2 5′ CS by rearranging the bases and altering its complementarity to the DENV 3′ UTR cyclization sequence. As a result, the binding was undetectable through MST (Fig. 1 *D*), confirming that the CS ultimately governs the association within DENV2 UTRs.

The cyclization of the DENV2 genome is a complex process that involves distal complementary sequences and *cis*-acting structural elements to support viral replication. In addition to both CSs, work on six different DENV2 isolates identified a high degree of conservation in the initial 300 nucleotides (50), which includes the full length of the 5′ region and almost the entire capsid protein-coding region. Furthermore, this research demonstrated that long-range RNA-RNA interactions between capsid-coding RNA and the duplicated dumbbell are critical for initiating genome cyclization. Meanwhile, utilizing a complete DENV2 sequence in a cellular system, a previous study demonstrated that the CSs are essential but not sufficient to maintain a circularized genome without the support of other elements, particularly the 5′ and 3′ UTRs (UARs) (9). Our in vitro binding studies meticulously examined the impact of exclusively disrupting the 5′ CS and the resultant biophysical effects on RNA-RNA interactions, thus reinforcing the notion that

Please cite this article in press as: Robinson et al., Structural dynamics of dengue virus UTRs and their cyclization, Biophysical Journal (2025), https://doi.org/10.1016/j.bpj.2025.09.004

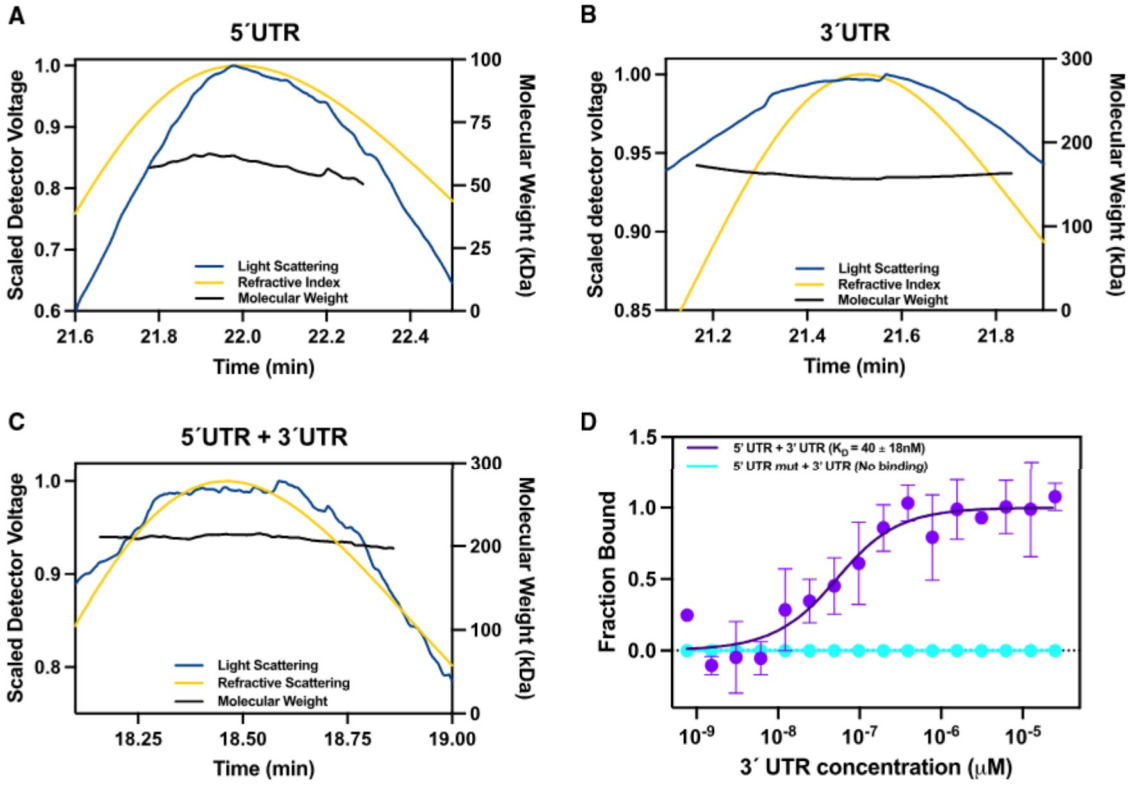

FIGURE 1 Purification and biophysical analysis of DENV 5′ and 3′ UTRs and their complex. Size-exclusion chromatography combined with multiangle light scattering (SEC-MALS) showed the absolute molar weight distribution for the 5′ UTR (*A*), 3′ UTR (*B*), and the 5′-3′ complex (*C*), displaying their respective elution profiles along with light scattering (*blue*), molar mass (*black*), and refractive index (*yellow*) signals. (*D*) Binding curves for DENV UTRs were obtained through microscale thermophoresis (MST), measuring the concentration versus fraction bound of the wild-type 5′-3′ complex (*purple*) compared with the 5′ cyclization mutant with the wild-type 3′ UTR (*blue*). MST experiments were performed in triplicate.

the CS is vital and that these RNAs cannot interact if the CS sequence is disrupted.

Structural characterization of DENV UTRs in solution

Due to the flexible nature of RNA-RNA complexes, structural characterization through traditional methods, such as cryo-electron microscopy and x-ray crystallography, is extremely challenging. For this reason, we chose to use size-exclusion chromatography coupled with small-angle x-ray scattering (SEC-SAXS) to obtain structural insights into DENV2 UTRs. SAXS is a low-resolution biophysical technique that provides valuable structural insights into RNA shape and conformation in solution (16,18,51–54). The elution profile for all studied RNAs demonstrated a single peak that was further analyzed (Fig. S2). The raw data for the 5′ UTR, 3′ UTR, and 5′-3′ complex (Fig. 2 *A*) were used to generate Guinier, Kratky, and P(r) plots. The Guinier analysis was used to assess the quality of the collected data. Due to this and the Gaussian nature of the largest peak on the SEC trace, we were confident that only or almost only 5′-3′ complex was present in the frames selected for analysis and proceeded accordingly. First, this analysis was used to determine the initial intensity (I(0)) and radius of gyration (R_g) values for each molecule (Table S2) (55,56). Subsequently, each plot was subjected to a linear regression. These linear regressions (Fig. 2 *B*), showed an absence of any upward or downward swing at the low-q range, indicating that the samples were free of aggregation and repulsive interparticle interactions that could affect the solution scattering profiles (57,58). Additionally, the overall linear nature of the points (Fig. 2 *B*) reinforced the monodispersity of the samples as previously shown using SEC-MALS. The quality of the fit between the linear regression and the plotted data served as an initial check to confirm the quality of the data (58–60). Next, using a dimensionless Kratky analysis, we assessed the folding of each molecule (60). After reaching a near-maximum, each of the three data sets exhibited a plateau-like distribution on the dimensionless Kratky plot (Fig. 2 *C*). This is indicative of an extended but folded conformation for all three RNAs, which agrees with the nature of noncoding RNAs as being extended and anisotropic molecules. Finally, we generated a pair distance distribution function (P(r)) that allowed for the calculation of reciprocal-space information (I(0) and R_g) and their maximum dimensions (D_{max}). The P(r) curves form symmetrical Gaussian distributions, which

Please cite this article in press as: Robinson et al., Structural dynamics of dengue virus UTRs and their cyclization, Biophysical Journal (2025), https://doi.org/10.1016/j.bpj.2025.09.004

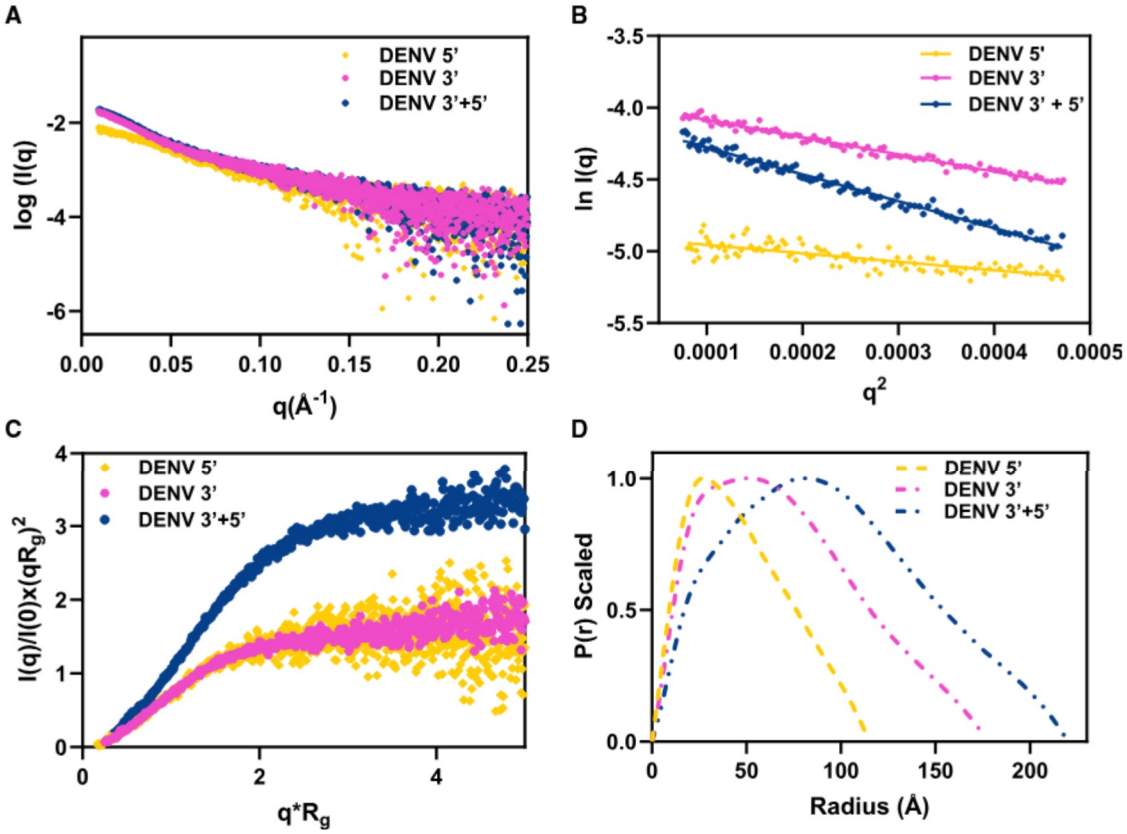

FIGURE 2 In-solution biophysical analysis of DENV RNAs using small-angle x-ray scattering. (*A*) Merged scattering data for the 5′ UTR (*yellow*), 3′ UTR (*pink*), and the 5′-3′ complex (*blue*) show the scattering intensity (log I(q)) plotted against the scattering angle ($q = 4\pi\sin\theta/\lambda$). (*B*) Guinier plots are used to determine the radius of gyration (R_g) from the low-angle region and assess the homogeneity of the samples. (*C*) Dimensionless Kratky plots $(I(q)/I(0) \times (q \times R_g)^2$ versus $q \times R_g)$ illustrate the elongated, non-Gaussian shape of the curve, which levels off into a plateau. (*D*) Normalized pair distance distribution plots facilitate the determination of the real-space R_g derived from the SAXS data set, including the D_{max} for each molecule.

corroborates the Kratky analysis and indicates that the molecules are elongated and anisotropic (Fig. 2 *D*). The molecular shape of our datasets was observed before as described (61). Additionally, the DENV2 3′ UTR (187.77 Å) has a larger D_{max} than the 5′ UTR (107.38 Å), as expected due to its larger length. Similarly, the complex (220.05 Å) presented a more extended molecule than the components alone.

Three-dimensional structures of DENV UTR revealed a dynamic arrangement of RNAs

The ab initio models for each molecule were generated from the P(r) curves using DAMMIN, followed by the derivation of an averaged filtered ab initio model utilizing DAMAVER. Overall, DAMMIN models align well with the P(r) information, as indicated by the low average χ^2 values of 1.125 and 1.040 for 5′ and 3′ UTR, respectively (Table S2). DAMAVER describes how well each model fits with the rest through the NSD parameter. NSD measures the quantitative similarity of overlapping molecules through three-dimensional points. It is determined by aligning two models and comparing the minimum distances between points in each model to assess dissimilarity. For the 5′ UTR, given its small length, all models were averaged and filtered, resulting in an NSD of 0.835 for all models (Table S2). This suggests a good agreement between the averaged structural representation and all individual 5′ UTR models. Fig. 3 *A* displays the filtered and averaged representative for the 5′ UTR. We have arbitrarily applied a Left and Right Arm label to the SAXS envelope for ease of reference. DENV 5′ UTR has an elongated RNA structure that is similar to other viral RNAs of comparable length (17,18,62). However, it shows a slight difference in the Left Arm, indicating a branched structure. Unsurprisingly, this branched structure was also characterized in DENV1 through high-resolution NMR spectroscopy and was described as an L-shaped structure (63). This structure encompasses the top and side of the 5′ stem-loop A (SLA), which is crucial for interacting with the viral polymerase NS5 to initiate viral RNA synthesis (64). Subsequently, we applied secondary structure constraints derived from probing techniques (14) to input data for calculating representative three-dimensional models. The secondary structure of the 5′ UTR is illustrated in Fig. 3 *B*, highlighting the SLA structure in black and the 5′ conserved sequence in green. A total of 2000

Please cite this article in press as: Robinson et al., Structural dynamics of dengue virus UTRs and their cyclization, Biophysical Journal (2025), https://doi.org/10.1016/j.bpj.2025.09.004

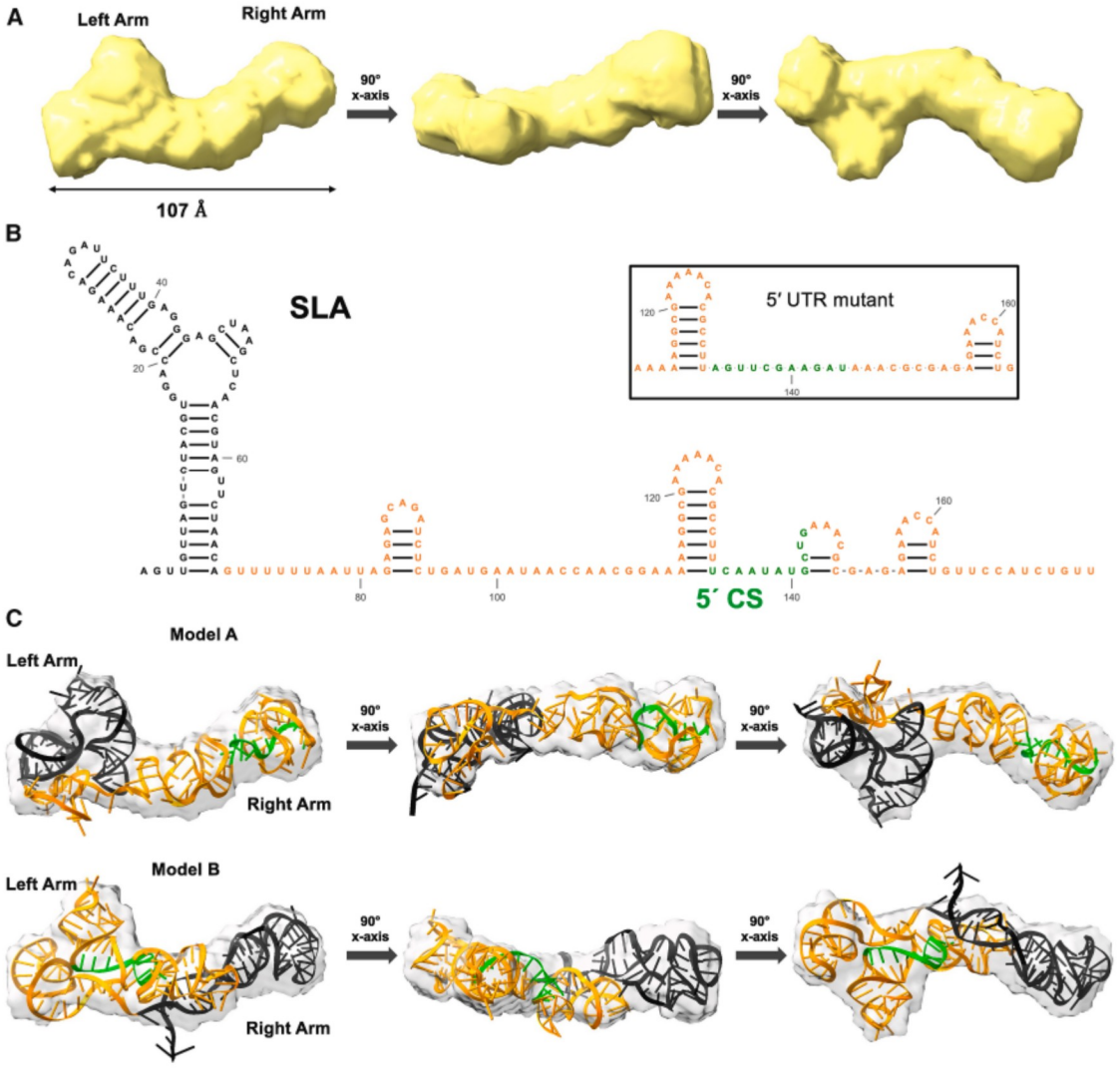

FIGURE 3 Structural characterization of DENV 5′ UTR. (*A*) The averaged low-resolution structure of the DENV 5′ UTR, determined using DAMAVER SAXS, displays an elongated, asymmetrical, and extended shape with a maximum length of 107.0 Å. (*B*) A secondary structure model for the DENV 5′ UTR is shown, highlighting the stem-loop A (SLA, *depicted in black*) and the cyclization sequence (CS, *depicted in green*). (*C*) All-atom, structure-based models of the DENV 5′ UTR were built. The fit of the computational models to the SAXS envelope was evaluated by calculating the normalized spatial discrepancies (NSD); the NSD values were 0.813 for model 1077 and 0.846 for model 1959.

coarse-grained three-dimensional models were generated using SimRNA. The best-fitting models were evaluated by calculating the NSD of the coarse-grained structures that overlapped with the SAXS envelopes (Fig. 3 *A*). The NSD values for all studied models are highlighted in Table S3. These values indicated minimal or nonsignificant discrepancies in both coarse-grained and SAXS models before MD simulations. Selected models (based on lower NDS and visual inspection) were then subjected to all-atom, structure-based modeling using MD to optimize their fitting within SAXS envelope constraints better.

To enhance the fitting, we employed MDfit-GROMACS, which facilitated folding of the simplified coarse-grained models within their respective electron density profiles. Two selected coarse-grained models (A and B) of the 5′ UTR, which demonstrated low NSD values compared with their SAXS envelope, underwent all-atom, structure-based modeling. A simulated map was created, and its correlation with the SAXS envelope was integrated into the potential energy function. These simulations were conducted over 200,000 steps to produce optimized models. Those all-atom models that depicted lower NSD values when superimposed with their SAXS envelope were further selected. The selected models exhibited lowered NSD values of 0.981 and 0.886 before MD for Model A and Model B, respectively (Table S3). After MD simulations, the two selected models exhibited NSD values of 0.813 and 0.846 for models A and B, respectively. These values indicated minimal or nonsignificant discrepancies in both coarse-grained and SAXS models, both before and after MD simulations. We apply

Please cite this article in press as: Robinson et al., Structural dynamics of dengue virus UTRs and their cyclization, Biophysical Journal (2025), https://doi.org/10.1016/j.bpj.2025.09.004

an additional series of definitional fitting parameters using ChimeraX 1.8 to assess the coarse-grained, all-atom structures fitting within the SAXS envelope and its correlation with the electron density map. Models A and B exhibited correlative fit values of 0.8628 and 0.8638, respectively, and "Fit-in-Map" values of 0.8787 and 0.8828, respectively, which demonstrated a strong correlation and a high degree of fit between the SAXS envelope and the all-atom, structure-based models (Fig. S3) (65).

Although each MD simulation does not represent a unique solution, nor is guaranteed to be a conformation consistently adopted by the 5′ UTR, we believe that insight can still be gained through examining the different conformations that the 5′ UTR can adopt within the density of our SAXS model. Model A illustrates the secondary structure of the SLA in black (Fig. 3 *C*), situated at the left-branched domain of the SAXS structure, as previously discussed.

In contrast, the 5′ CS, in green, is located at the opposite end of the envelope. This L-shaped configuration may facilitate the binding of the NS5 protein before synthesizing the negative strand of the viral genome. On the other hand, model B represents a structure where the SLA is in a linear, extended region without any branched domain (Fig. 3 *C*). In this model, 5′ CS is positioned at the center of the left-branched envelope, making it less accessible for binding with the 3′ CS. Overall, these two models illustrate different structural arrangements for the 5′ UTR, which consequently influence the cyclization mechanism. Model A aligns well with the common understanding that the SLA forms an L-shaped structure, allowing the cyclization sequence to be more readily available for binding with the 3′ CS. Notably, another study has shown that *Flavivirus* evolution has developed a Y-shaped topology in its 5′ UTR, and this region directly influences viral pathogenesis (66). In contrast, model B presents a less conventional arrangement where the 5′ CS is "protected," and the SLA is linear. This suggests that the 5′ UTR could surround the 5′ CS in a manner that prevents nonspecific binding, subsequently inhibiting the replication of DENV. This would be an interesting model to investigate using single-molecule techniques such as fluorescence resonance energy transfer.

Considering the size and structural complexity of the 3′ UTR and 5′-3′ UTR complex, we decided to cluster DAMMIN models to obtain a more accurate representation of the structural conformations using DAMCLUST. This program is primarily used to cluster multiple bead model reconstructions generated from SAXS data, which demonstrate a similar overall structure but exhibit some heterogeneity (67). The analysis of DENV 3′ UTR structures was grouped in four prominent clusters accounting for Cluster 1 (C1, 34%), C2 (24%), C3 (12%), and C4 (8%) of the total models (Fig. 4 *A*). In each case the DAMCLUST software selected the model that was most representative of the cluster of similar models based on NSD values. A visual inspection was also performed on each model, using ChimeraX, to ensure that they make sense and overlap with the SAXS envelope. Clusters that represented less than 5% of the total models were not shown. Identifying distinct clusters for the 3′ UTR demonstrates its flexibility, highlighting the multiple conformations it can adopt. However, several similarities can be observed between them, such as their relatively compact structure with a central protrusion. Although DENV and JEV belong to the mosquito-borne flaviviruses and share equivalent structures in their 3′ UTR (68), our study highlights structural differences in DENV conformation when compared with those previously reported for the JEV 3′ UTR (18). Although all DENV conformations have middle protrusions and less-extended structures (187.0 Å), JEV structures have protrusions closer to the RNA horizontal extremities and a very elongated structure (345.0 Å). In previous studies, researchers failed to obtain a unique SAXS envelope representing the topological structures for DENV, ZIKV, and WNV 3′ UTRs (69). Our study also does not provide a single representation for DENV 3′ UTR. Instead, we acknowledge the innate plasticity of this RNA and provide a clustered consideration encompassing several of the likely ab initio representations and conformations it can adopt.

Next, we utilized constraints from secondary structures, as represented in Fig. 4 *B* (14), to calculate three-dimensional structures for DENV 3′ UTR using SimRNA, as was done for the 5′ UTR. After this, MD simulations were conducted for 200,000 steps to generate optimized, all-atom structure-based models. The overlap of these models with their respective SAXS envelopes was assessed using the DAMSUP tool, and an NSD value was calculated before and after MD simulation (Table S3). As illustrated in Fig. 4 *B*, the 3′ UTR does not have a polyA tail and features repeated structures, which include two stem-loops (SLI and SLII, in blue), two dumbbells (DBI and DBII, in gray), a short hairpin (sHP), and a third stem-loop (SLIII, in purple), as previously reported (68). The calculated NSDs for Cluster 1 Model A (C1-A), C2-B, C3-C, and C4-D are 0.838, 0.804, 0.770, and 0.785, respectively, which indicates a strong fit. Further, all-atom, structure-based modeling of the coarse-grained models improved the correlative fit and "Fit-in-Map" values of the 3′ UTR models, demonstrating a strong degree of fit with values above 0.85 (Fig. S3). The Cluster 1 Model A featured an elongated linear structure in the left arm that accommodates the duplicated SLI and SLII. In contrast, the dumbbells are centrally located in a compact curved shape, followed by the sHP SLIII in the right arm (Fig. 5 *A*). Additionally, the 3′ CS is exposed at the surface, surrounded by sHP SLIII, which consists of an almost complete double-stranded RNA. This further indicates the absence of nearby regulatory single-stranded

Please cite this article in press as: Robinson et al., Structural dynamics of dengue virus UTRs and their cyclization, Biophysical Journal (2025), https://doi.org/10.1016/j.bpj.2025.09.004

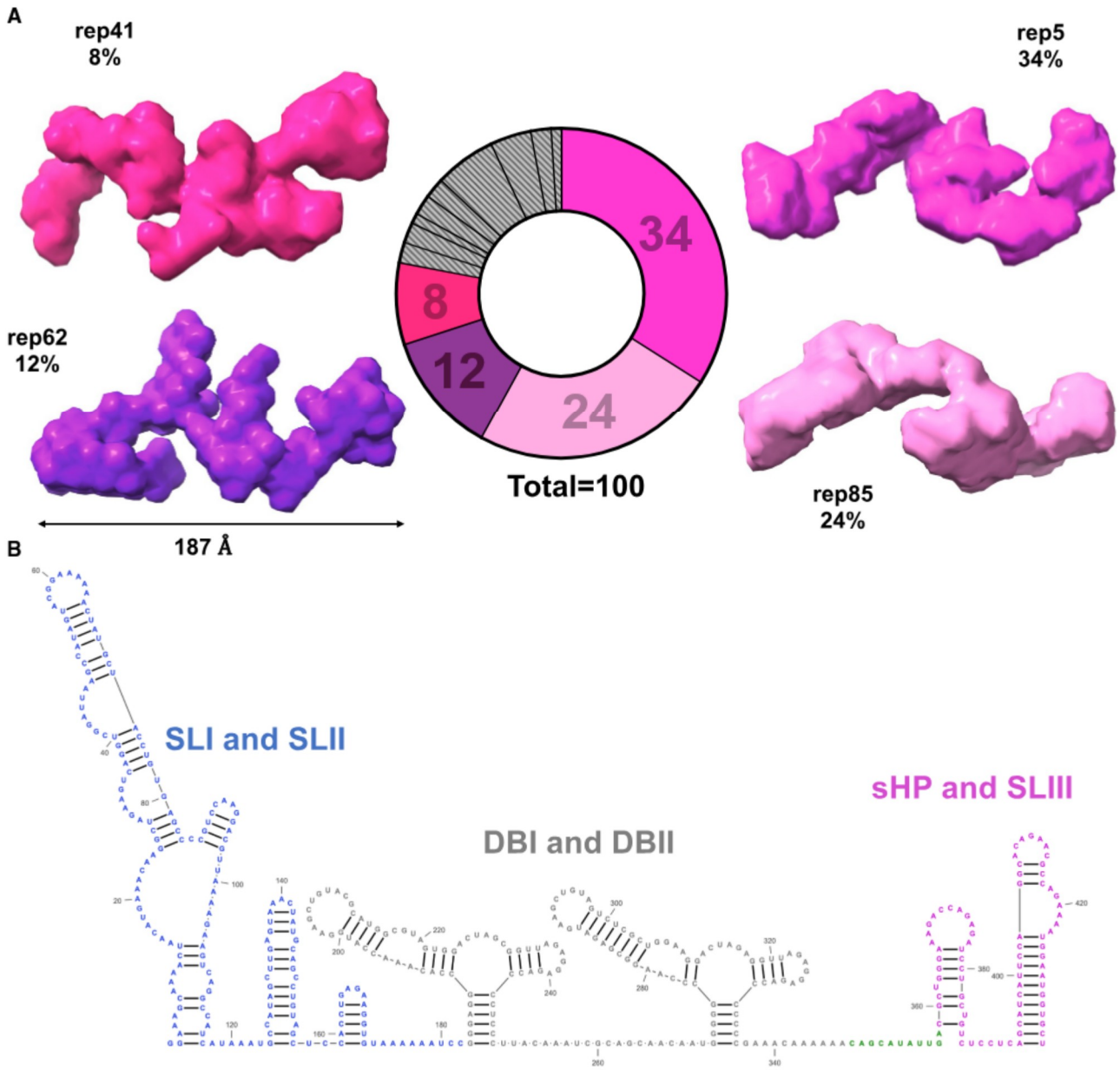

FIGURE 4 Structural investigation of DENV 3′ UTR. (*A*) A clustering analysis of the DENV 3′ UTR was performed using DAMCLUST. One hundred DAMMIN models were grouped into clusters based on structural similarities, represented as percentages. Four predominant clusters were identified. This analysis highlights the structural flexibility of the various conformations adopted by this RNA. (*B*) A secondary structure model of the DENV 3′ UTR is shown. The model emphasizes the duplicated stem-loops (SLI and SLII, *shown in blue*), the duplicated dumbbells (DBI and DBII, *shown in gray*), and the short hairpin and stem-loop three (sHP/SLIII, *shown in purple*).

sites adjacent to the CS in Cluster 1 Model A. A prior study revealed that the duplicated dumbbells contain sequences that overlap with the 3′ UTR CS, thereby impairing viral replication (70). Although these structures are nonunique in nature and the fit between the MD simulations and SAXS models can only be evaluated at the low resolution of the SAXS models, these results are the first of their kind to suggest the unique evolution of these RNA structures in modulating viral replication across different hosts.

The following models (Cluster 2 Model B and Cluster 3 Model C) illustrate a new rearrangement of the DENV 3′ UTR, where the duplicated stem-loops are positioned on the right side of the envelope, and the sHP SLIII is situated on the left side. Although the 3′ CS is more exposed in Cluster 2 Model B (Fig. 5 *B*), the spatial distance between the two models suggests that there may be no direct regulation of the CS. In Cluster 2 Model B (Fig. 5 *C*), the 3′ CS is surrounded by the sHP SLIII, making it inaccessible for regulating DBI and DBII. Interestingly, Cluster 4 Model D

Please cite this article in press as: Robinson et al., Structural dynamics of dengue virus UTRs and their cyclization, Biophysical Journal (2025), https://doi.org/10.1016/j.bpj.2025.09.004

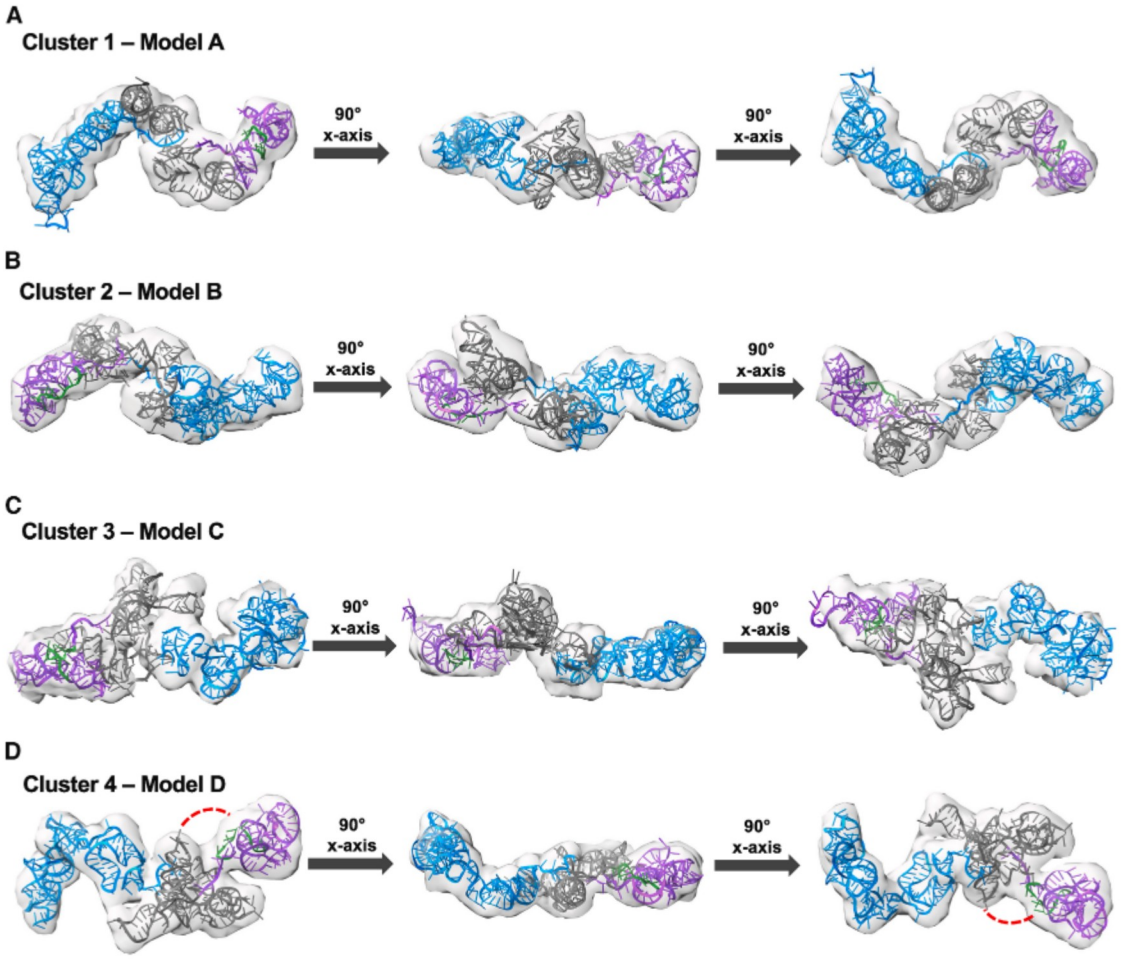

FIGURE 5 Optimized coarse-grained models for DENV 3′ UTR. Representative models showing better overlap within clustered SAXS models for the DENV 3′ UTR were analyzed. A total of 2000 SimRNA models were generated by applying secondary structure constraints. These models were then screened for the best fit using the NSD, followed by all-atom, structure-based modeling with MDfit-GROMACS molecular dynamics simulations. The calculated NSD values after the simulations were 0.838 for Cluster 5 with Model 1446 (*A*), 0.804 for Cluster 41 with Model 957 (*B*), 0.770 for Cluster 62 with Model 1030 (*C*), and 0.785 for Cluster 85 with Model 978 (*D*).

highlights the proximity of the apical loop of DBII to the exposed 3′ UTR CS (as indicated by the dashed lines in Fig. 5 *D*). This helps affirm a model for the tight regulation of viral replication wherein UTR structures influence viral lifecycle as formerly explained by CS mechanistic studies (70). Additionally, this model features a curved stem-loop in the left arm of the SAXS envelope, along with a condensed dumbbell structure located in the center. The sHP SLIII fits into a protrusion on the right side of the envelope. In summary, these models offer a potential explanation for how different structural states can influence viral replication through its CS. However, multiple host factors, specifically RBPs, could contribute to this structural configuration. Identification of these putative regulatory sites sets the stage for pulldown experiments to identify binders to these very specific regions of the UTRs, to discover novel proteins that may play a key role in regulating viral replication.

Structural plasticity of DENV UTRs in complex provides insight into the viral replication mechanism

We sought to better understand the SAXS structural conformations for the complex by collecting data from a 1:1 mixture of the 5′ and 3′ UTR solutions. Due to its size and subsequent flexibility, we generated 100 DAMMIN models of the 3′ UTR and then clustered them using DAMCLUST (Fig. 6). We identified four main clusters that accounted for 62% of the models. This included Complex I (25%), Complex II (23%), Complex III (12%), and Complex IV (12%). Clusters representing less than 10% of the total data were discarded. We observed a significant conformational change when the DENV UTRs formed a complex. This complex displayed reduced flexibility and a noticeably linear extended domain branched at the center of the envelope.

Please cite this article in press as: Robinson et al., Structural dynamics of dengue virus UTRs and their cyclization, Biophysical Journal (2025), https://doi.org/10.1016/j.bpj.2025.09.004

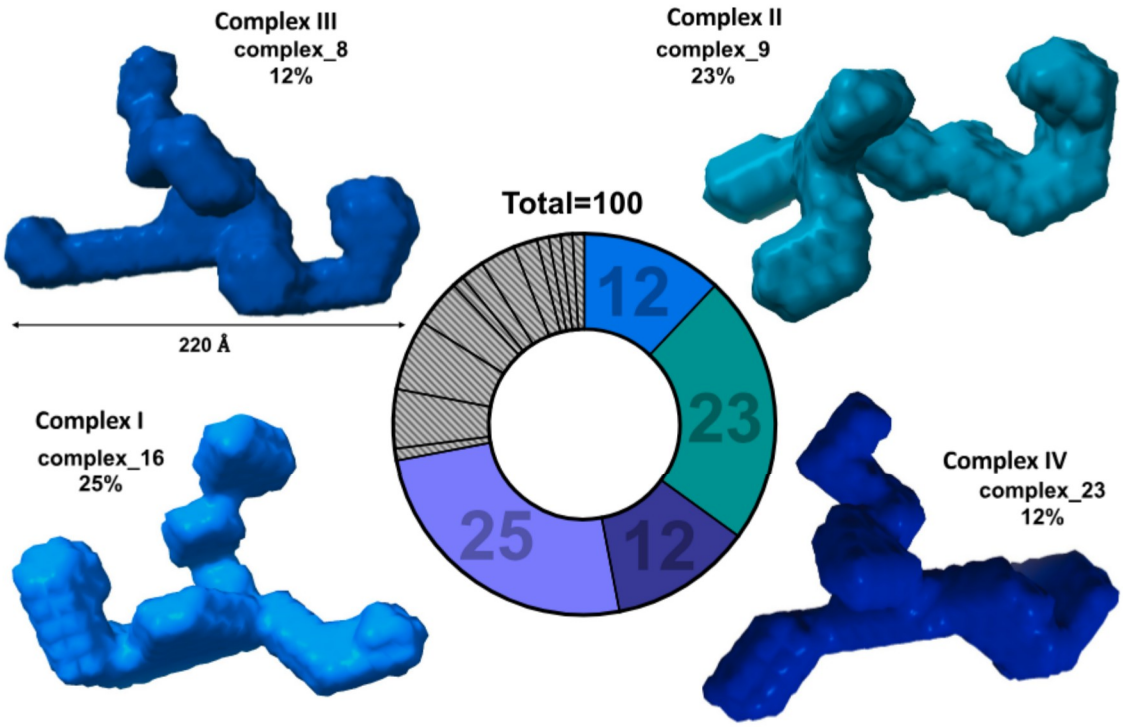

FIGURE 6 Low-resolution structural analysis of the DENV 5′-3′ UTR complex. A clustering analysis of the DENV 5′-3′ UTR complex was conducted using DAMCLUST. A total of one hundred DAMMIN models were grouped into clusters based on their structural similarities, represented as percentages. Four main clusters were identified.

Additionally, a right arm was consistently seen in complexes II, III, and IV, whereas in Complex I, this arm was located at the left end of the envelope. A previous study conducted an RNA-RNA biophysical characterization of JEV UTRs, revealing a significantly extended structure (410 Å) with notable differences in the central pockets and terminal protrusions (18). The UTRs of DENV and JEV share some similarities as members of the *Flavivirus* genus but exhibit notable differences in their structures and functions. JEV has a 300-nucleotide variable region at the beginning of the 3′ UTR, forming four stem-loop structures (SLI—SLIV), which are characteristic of encephalitic flaviviruses (71). In contrast, DENV's 3′ UTR lacks these specific encephalitic flavivirus-associated structures and only forms SLI and SLII. Collectively, these differences in sequence and structure account for the unique features observed in the SAXS envelopes of DENV and JEV. To our knowledge, this is the first structural and biophysical investigation of DENV UTRs in cyclization to have been published to date.

Due to the low resolution of SAXS models, it is unreasonable to determine the orientation of the molecules and the domains involved in binding solely based on the three-dimensional envelope. To gain more structural insights into DENV cyclization, we performed MD simulations. MDfit was used in a comparable manner to that employed for both the 5′ and 3′ UTRs. However, there were no available secondary structure constraints for this RNA-RNA complex to define orientation and directionality. Based on our MST data, we anticipated that the interaction between both CSs is essential for forming the RNA-RNA complex.

Additionally, a preliminary study elucidated that UAR basepairing is necessary for the *trans*-initiation activity of the viral polymerase NS5, which initiates genome replication (8). To address this, we designed a unique secondary structure profile for a co-fold between the 5′ and 3′ UTRs as a single molecule. This, in turn, mimics a full-length viral genome during replication. We maintained their known secondary structure properties and all cis-acting elements that were previously demonstrated to be critical for genome circularization while incorporating mandatory constraints for viral cyclization, such as the CS and UAR basepairing. Four thousand coarse-grained SimRNA models were generated, and the models that demonstrated best fits (based on NSD before MD and visual inspection) were further optimized through MD simulations, with NSD calculated using DAMSUP.

The best model for each complex is illustrated in Fig. 7 with NSDs for Complex I Model A being 0.833, Complex II Model B being 0.824, Complex III Model C being 0.808, and Complex IV Model D being 0.937, as demonstrated in Table S3. All-atom, structure-based modeling additionally improved the correlative fit and "Fit-in-Map" values of the complexes' models, creating a high degree of fit with values above 0.8 (Fig. S3). The 5′ UTR is represented in orange. At the same time, the DENV 3′ UTR is shown in purple, and the CS sequences are in green. The

Please cite this article in press as: Robinson et al., Structural dynamics of dengue virus UTRs and their cyclization, Biophysical Journal (2025), https://doi.org/10.1016/j.bpj.2025.09.004

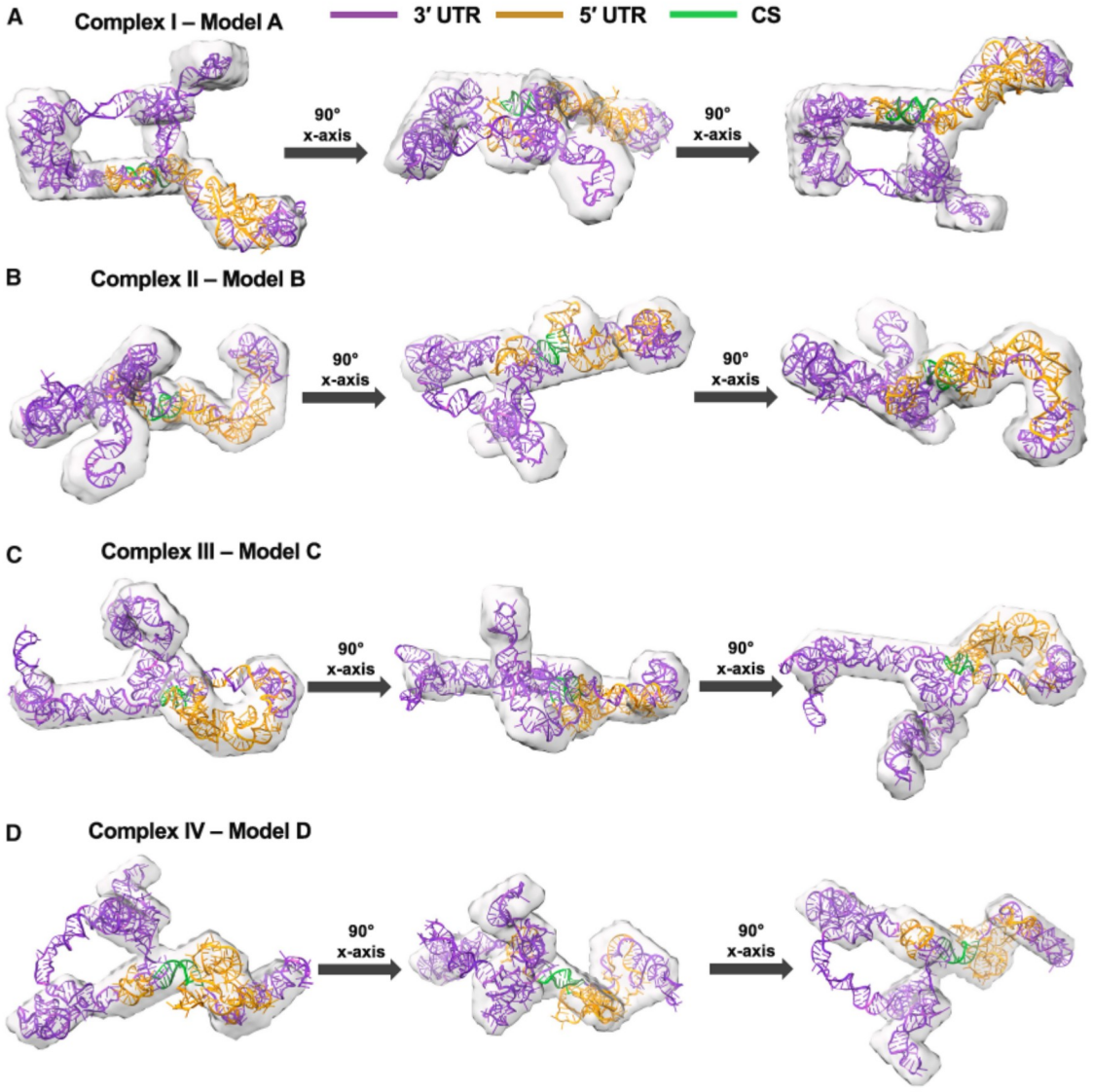

FIGURE 7 Optimized coarse-grained models generated for the DENV 5′-3′ UTR complex. We examined representative models that showed better overlap within clustered SAXS models for the DENV 5′-3′ UTR complex. A total of 4000 SimRNA models were created, preserving key secondary structures and incorporating a cyclization sequence along with a UAR basepair, which served as an additional constraint for the co-fold model. The best coarse-grained models were then assessed for the optimal fit using the NSD, followed by all-atom, structure-based modeling with MDfit-GROMACS molecular dynamics simulations. The calculated NSD values after the simulations were as follows: 0.808 for Cluster 8 with Model 2731 (*A*), 0.824 for Cluster 9 with Model 3674 (*B*), 0.833 for Cluster 16 with Model 3739 (*C*), and 0.937 for Cluster 23 with Model 3737 (*D*).

branched L-shaped domain of the 5′ UTR compacts when basepairing occurs within the CSs and UARs. Complex I Model A (Fig. 7 *A*) exhibited a more distinctive structure, characterized by a long overlapping region observed within the 5′ and 3′ UTR, which extends from the center to the bottom right side of the model. As seen in the previous models, the central protrusion primarily accommodates a branched 3′ UTR. Complex I Model A showed a good dimensional fit within the SAXS envelope, with only a minimal double-stranded region left uncovered.

Due to the indeterminate resolution of the SAXS models, the volume map could be expanded to encompass this loop-like structure. However, we use the same volume map for all SAXS models to maintain consistency and provide room for the RNAs' dynamic conformational flexibility to perform in solution (72,73). In Complex II Model B (Fig. 7 *B*), the 5′ and 3′ UTRs have minimal overlapping points, with a small loop in the 3′ UTR located at the right end. Instead of the boomerang shape, the 3′ UTR exhibited a curved structure that is bidirectionally branched at the middle protrusion. A boomerang-like shape was observed for the 3′ UTR in Complex III Model C (Fig. 7 *C*), which extended from the left end of the SAXS envelope to the middle protrusion. There were minimal overlapping points between the 5′ and 3′ UTRs, whereas the CS hybridization is at the structure's core. SAXS dimensions for both RNAs generally aligned

Please cite this article in press as: Robinson et al., Structural dynamics of dengue virus UTRs and their cyclization, Biophysical Journal (2025), https://doi.org/10.1016/j.bpj.2025.09.004

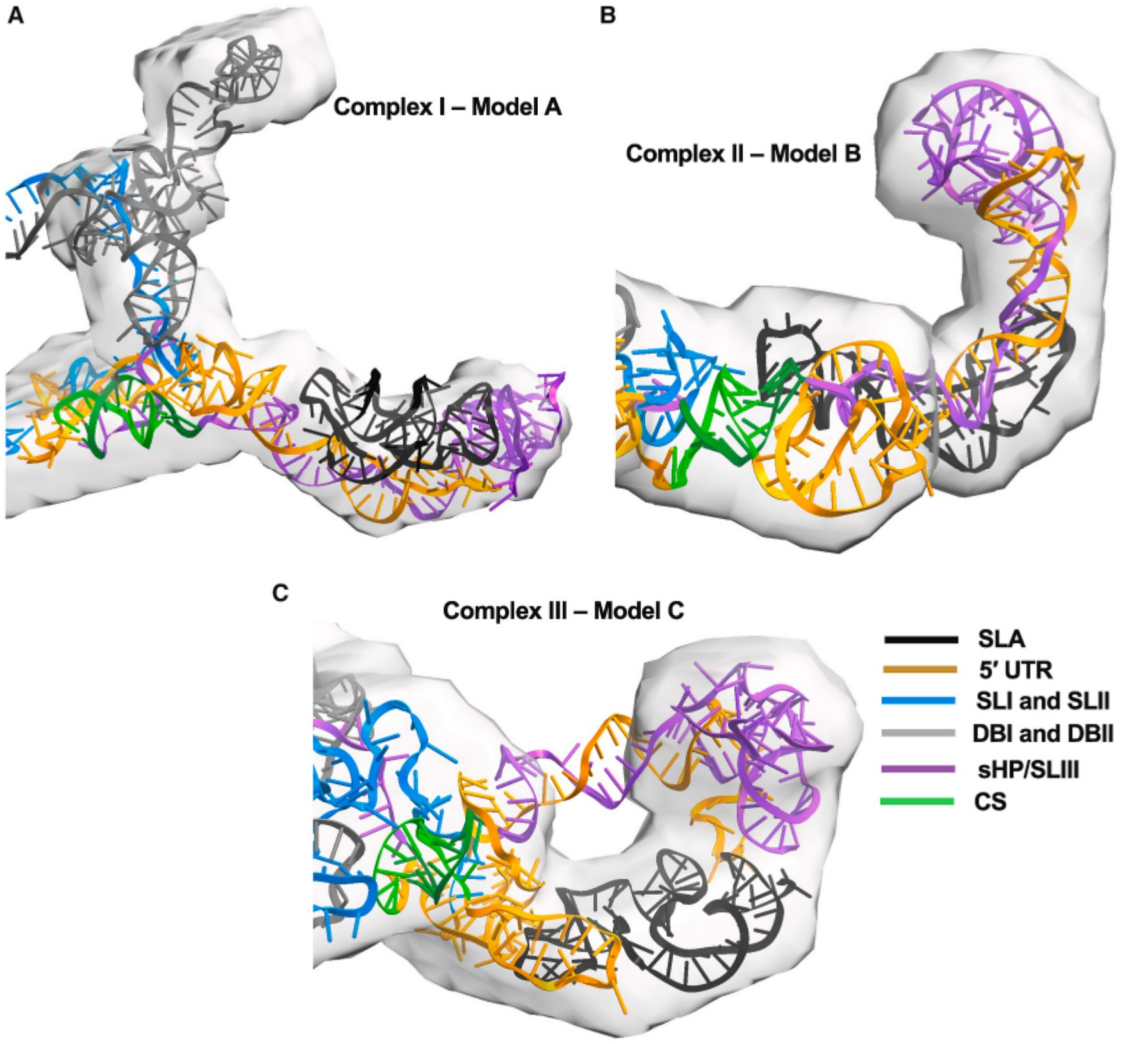

FIGURE 8 Extended depiction of the DENV 5′-3′ UTR complex, showing the detailed structural arrangement around the cyclization sequence. (*A*) The c8_model2731 presents the RNA-RNA complex in a closed form, whereas (*B*) c9_model3674 and (*C*) c16_model3739 display an open and transitional conformation, respectively. The 5′ UTR is shown in orange, with the SLA and 5′ CS highlighted in black and green. Additionally, the main structural domains of the 3′ UTR are depicted in blue, gray, and purple to illustrate the duplicated stem-loops, duplicated dumbbells, and sHP/SLIII, respectively.

well with the coarse-grained models, with only a few exceptions for the top loop on the left side and UAR hybridization (indicated by purple and orange basepairing). Consequently, this shows a good fit between the models. The SAXS model's dimensions for this structure also agreed with the coarse-grained models. Much like the Complex I Model A, Complex IV Model D (Fig. 7 *D*) also exhibits a distinctive structure, characterized by long overlapping regions within the 5′ and 3′ UTRs. In contrast, Complex IV Model D, as further reflected by its NSD measurement, has a long loop not included within the SAXS envelope, consequently diminishing its agreement and structural fidelity.

To gain further insights into how these models represent structural domains when both UTRs are cyclized, we present a zoomed-in view of the adjacent structures surrounding the CS basepair (Fig. 8). Fig. 8 *A* and *B* depict the right branch of the SAXS structure, which represents an open structure that maintains the same 5′ SLA, 3′ sHP/SLIII, and UAR basepairing. Notably, the Complex I Model A features a wide-open branched structure that encompasses the dumbbells (gray) and SLII (light blue), suggesting a potential site accommodating host or viral proteins. In contrast, Fig. 8 *C* shows that the same right branch of the SAXS structure predominantly accommodates the 5′ SLA and 3′ sHP/SLIII, along with their interaction through the UAR (orange-purple basepair), assuming a closed conformation. For this reason, we believe that this region is of interest as a potential binding site for a regulatory element. Interestingly, this structural transition from a closed to an open conformation was previously hypothesized through a de novo synthesis of viral negative strands (74). Although the precise conformational changes in RNA structures during cyclization and NS5 binding remain unclear, and it is unlikely that our models describe all possible conformations

of the complex, it is plausible that these models represent multiple conformations that DENV UTRs might assume when cyclized. The mechanism by which DENV NS5 initiates the synthesis of the negative strand of the viral genome involves a combination of RNA structural elements and specific interactions with NS5's RNA-dependent RNA polymerase and methyltransferase domains (75), along with unwinding secondary structure known to promote viral cyclization (76). NS5 binds specifically to the SLA via its RNA-dependent RNA polymerase domain to initiate de novo RNA synthesis and genome cyclization, which is believed to facilitate the transfer of NS5 from the 5′ SLA to the 3′ end initiation site (77). Although the significance of the SLA promoter is well established, the potential roles of other RNA secondary structures in fine-tuning initiation have not been thoroughly examined. We hypothesize that these three models can enhance our understanding of NS5 binding when the DENV genome is cyclized, providing temporal and structural insights into other elements that support viral replication. The duplicated dumbbells are relocated to a distal branch, forming an open clamp-like structure that may accommodate NS5 and potentially facilitate the unzipping of the genome to synthesize the negative strand (Fig. 8 *A*). Subsequently, the 5′ SLA and 3′ sHP/SLIII are rearranged to the right arm of the SAXS envelope upon "opening" the circular structure (Fig. 8 *B*). Finally, the closed model depicted in Fig. 8 *C* may indicate a viral genome that comes into proximity immediately after cyclization and UAR basepairing.

CONCLUSIONS

Our research combines biophysical and computational techniques to offer significant insights into the key interactions involved in DENV replication. The results from our comprehensive biophysical analysis show that our methods effectively characterize the interactions of DENV UTRs and measure their binding affinity in solution. We also provide a three-dimensional depiction of individual UTRs and the associated complexes, proposing a flexible and dynamic model to explain the organization of DENV UTRs. Additionally, we have developed computational models that incorporate known secondary structure constraints to highlight important elements involved in viral cyclization. These models suggest various organizational patterns that demonstrate the plasticity of DENV UTRs and outline a temporal mechanism for NS5 binding before the synthesis of the negative strand of the DENV genome. Furthermore, in vivo studies on the structures of the DENV UTR and their role in CS basepairing and NS5 processivity are crucial for understanding various events in the viral lifecycle, particularly viral replication. Ultimately, our research provides valuable insights into the structural organization of DENV cyclization, which could contribute to the development of anti-DENV therapeutics.

DATA AVAILABILITY

SAXS samples are available at the Small Angle Scattering Biological Data Bank (SASBDB) using the following links (78):

5′ UTR: https://www.sasbdb.org/data/SASDXT3/gj1f8ku13w

3′ UTR: https://www.sasbdb.org/data/SASDXD3/vz08y85rhk/

5′-3′ complex: https://www.sasbdb.org/data/SASDXE3/peswlglctz/

ACKNOWLEDGMENTS

H.S.P is supported by the Alberta Innovates Postdoctoral Fellowship. M.H.D. is supported by an NSERC Discovery grant awarded to T.R.P. M.H.D. is supported by The King's Own Calgary Regiment (RCAC) Funds Foundation, Canada; the Canadian Armed Forces Individual Learning Plan and Self-Development Program, Canada; and the Canadian Institute of Health Research, Canada (CIHR) CGS-D Award, Canada. T.R.P. is a Canada Research Chair in RNA and Protein Biophysics. We acknowledge infrastructure support from NSERC RTI and CFI grants. The SAXS data collection was supported by Diamond Light Source, UK. We would additionally like to thank the B21 beamline scientists at Diamond Light Source for their continual support.

AUTHOR CONTRIBUTIONS

Z.E.R. and H.S.P. performed the majority of the experiments, and M.H.D. performed MD analysis. T.R.P. secured funds and supervised the project. All authors contributed to manuscript writing.

DECLARATION OF INTERESTS

The authors declare no competing interests.

SUPPORTING MATERIAL

Supporting material can be found online at https://doi.org/10.1016/j.bpj.2025.09.004.

REFERENCES

1. van den Elsen, K., B. L. A. Chew, …, D. Luo. 2023. Flavivirus nonstructural proteins and replication complexes as antiviral drug targets. *Curr. Opin. Virol.* 59:101305.
2. van Leur, S. W., T. Heunis, …, S. Sanyal. 2021. Pathogenesis and virulence of flavivirus infections. *Virulence.* 12:2814–2838.
3. World Health Organization. 2025. Dengue. https://www.who.int/news-room/fact-sheets/detail/dengue-and-severe-dengue.
4. Yamashita, A., T. Sakamoto, …, M. Kuroda. 2016. DGV: Dengue Genographic Viewer. *Front. Microbiol.* 7:875.
5. Gupta, A., P. Rijhwani, …, R. K. Jat. 2021. Prevalence of Dengue Serotypes and Its Correlation With the Laboratory Profile at a Tertiary Care Hospital in Northwestern India. *Cureus.* 13:e15029.
6. Soo, K. M., B. Khalid, …, H. Y. Chee. 2016. Meta-Analysis of Dengue Severity during Infection by Different Dengue Virus Serotypes in Primary and Secondary Infections. *PLoS One.* 11:e0154760.

7. Vicente, C. R., K. H. Herbinger, …, C. Cerutti Junior. 2016. Serotype influences on dengue severity: a cross-sectional study on 485 confirmed dengue cases in Vitoria, Brazil. *BMC Infect. Dis.* 16:320.
8. Alvarez, D. E., C. V. Filomatori, and A. V. Gamarnik. 2008. Functional analysis of dengue virus cyclization sequences located at the 5' and 3'UTRs. *Virology.* 375:223–235.
9. Alvarez, D. E., M. F. Lodeiro, …, A. V. Gamarnik. 2005. Long-range RNA-RNA interactions circularize the dengue virus genome. *J. Virol.* 79:6631–6643.
10. Kok, B. H., H. T. Lim, …, C. H. Leow. 2023. Dengue virus infection - a review of pathogenesis, vaccines, diagnosis and therapy. *Virus Res.* 324:199018.
11. Kariyawasam, R., M. Lachman, …, A. K. Boggild. 2023. A dengue vaccine whirlwind update. *Ther. Adv. Infect. Dis.* 10:204993612 31167274.
12. Thomas, S. J. 2023. Is new dengue vaccine efficacy data a relief or cause for concern? *NPJ Vaccines.* 8:55.
13. Allen, T., M. E. Castellanos, …, S. Pai. 2024. Next-generation vaccines for tropical infectious diseases. *Int. J. Infect. Dis.* 143:107014.
14. Huber, R. G., X. N. Lim, …, Y. Wan. 2019. Structure mapping of dengue and Zika viruses reveals functional long-range interactions. *Nat. Commun.* 10:1408.
15. Kinney, R. M., S. Butrapet, …, D. J. Gubler. 1997. Construction of infectious cDNA clones for dengue 2 virus: strain 16681 and its attenuated vaccine derivative, strain PDK-53. *Virology.* 230:300–308.
16. D'Souza, M. H., T. Mrozowich, …, T. R. Patel. 2022. Biophysical characterisation of human LincRNA-p21 sense and antisense Alu inverted repeats. *Nucleic Acids Res.* 50:5881–5898.
17. Mrozowich, T., A. Henrickson, …, T. R. Patel. 2020. Nanoscale Structure Determination of Murray Valley Encephalitis and Powassan Virus Non-Coding RNAs. *Viruses.* 12:190.
18. Mrozowich, T., S. M. Park, …, T. R. Patel. 2023. Investigating RNA-RNA interactions through computational and biophysical analysis. *Nucleic Acids Res.* 51:4588–4601.
19. Mann, M., P. R. Wright, and R. Backofen. 2017. IntaRNA 2.0: enhanced and customizable prediction of RNA-RNA interactions. *Nucleic Acids Res.* 45:W435–W439.
20. Moon, M. H., T. A. Hilimire, …, J. S. Schneekloth, Jr. 2018. Measuring RNA-Ligand Interactions with Microscale Thermophoresis. *Biochemistry.* 57:4638–4643.
21. Meier, M., A. Moya-Torres, …, J. Stetefeld. 2018. Structure and hydrodynamics of a DNA G-quadruplex with a cytosine bulge. *Nucleic Acids Res.* 46:5319–5331.
22. Manalastas-Cantos, K., P. V. Konarev, …, D. Franke. 2021. ATSAS 3.0: expanded functionality and new tools for small-angle scattering data analysis. *J. Appl. Crystallogr.* 54:343–355.
23. Panjkovich, A., and D. I. Svergun. 2018. CHROMIXS: automatic and interactive analysis of chromatography-coupled small-angle X-ray scattering data. *Bioinformatics.* 34:1944–1946.
24. Putnam, C. D. 2016. Guinier peak analysis for visual and automated inspection of small-angle X-ray scattering data. *J. Appl. Crystallogr.* 49:1412–1419.
25. Burke, J. E., and S. E. Butcher. 2012. Nucleic acid structure characterization by small angle X-ray scattering (SAXS). *Curr. Protoc. Nucleic Acid Chem.* Chapter 7:Unit 7.18.
26. Semenyuk, A. V., and D. I. Svergun. 1991. Gnom - a Program Package for Small-Angle Scattering Data-Processing. *J. Appl. Crystallogr.* 24:537–540.
27. Svergun, D. I. 1992. Determination of the Regularization Parameter in Indirect-Transform Methods Using Perceptual Criteria. *J. Appl. Crystallogr.* 25:495–503.
28. Svergun, D. I. 1999. Restoring low resolution structure of biological macromolecules from solution scattering using simulated annealing. *Biophys. J.* 76:2879–2886.
29. Volkov, V. V., and D. I. Svergun. 2003. Uniqueness of shape determination in small-angle scattering. *J. Appl. Crystallogr.* 36:860–864.
30. Boniecki, M. J., G. Lach, …, J. M. Bujnicki. 2016. SimRNA: a coarse-grained method for RNA folding simulations and 3D structure prediction. *Nucleic Acids Res.* 44:e63.
31. Volkov, V. V., and D. I. Svergun. 2003. Uniqueness of ab initio shape determination in small-angle scattering. *J. Appl. Crystallogr.* 36:860–864.
32. Kozin, M. B., and D. I. Svergun. 2001. Automated matching of high- and low-resolution structural models. *J. Appl. Crystallogr.* 34:33–41.
33. Pettersen, E. F., T. D. Goddard, …, T. E. Ferrin. 2004. UCSF Chimera–a visualization system for exploratory research and analysis. *J. Comput. Chem.* 25:1605–1612.
34. Kim, D. N., N. W. Moriarty, …, K. Sanbonmatsu. 2019. Cryo_fit: Democratization of flexible fitting for cryo-EM. *J. Struct. Biol.* 208:1–6.
35. Lemkul, J. A. 2024. Introductory Tutorials for Simulating Protein Dynamics with GROMACS. *J. Phys. Chem. B.* 128:9418–9435.
36. de Oliveira, A. B., Jr., V. G. Contessoto, …, P. C. Whitford. 2022. SMOG 2 and OpenSMOG: Extending the limits of structure-based models. *Protein Sci.* 31:158–172.
37. Noel, J. K., M. Levi, …, P. C. Whitford. 2016. SMOG 2: A Versatile Software Package for Generating Structure-Based Models. *PLoS Comput. Biol.* 12:e1004794.
38. Ratje, A. H., J. Loerke, …, C. M. T. Spahn. 2010. Head swivel on the ribosome facilitates translocation by means of intra-subunit tRNA hybrid sites. *Nature.* 468:713–716.
39. Wriggers, W. 2012. Conventions and workflows for using Situs. *Acta Crystallogr. D Biol. Crystallogr.* 68:344–351.
40. Hess, B., C. Kutzner, …, E. Lindahl. 2008. GROMACS 4: Algorithms for Highly Efficient, Load-Balanced, and Scalable Molecular Simulation. *J. Chem. Theor. Comput.* 4:435–447.
41. Pall, S., A. Zhmurov, …, E. Lindahl. 2020. Heterogeneous parallelization and acceleration of molecular dynamics simulations in GROMACS. *J. Chem. Phys.* 153:134110.
42. Pronk, S., S. Páll, …, E. Lindahl. 2013. GROMACS 4.5: a high-throughput and highly parallel open source molecular simulation toolkit. *Bioinformatics.* 29:845–854.
43. Kim, I., S. A. McKenna, …, J. D. Puglisi. 2007. Rapid purification of RNAs using fast performance liquid chromatography (FPLC). *RNA (N. Y.).* 13:289–294.
44. Badmalia, M. D., M. Q. Siddiqui, …, T. R. Patel. 2020. Analytical ultracentrifuge: an ideal tool for characterization of non-coding RNAs. *Eur. Biophys. J.* 49:809–818.
45. De Vos, J., K. Morreel, …, K. Sandra. 2024. Evaluation of size-exclusion chromatography, multi-angle light scattering detection and mass photometry for the characterization of mRNA. *J. Chromatogr. A.* 1719:464756.
46. Wyatt, P. J. 1993. Light-Scattering and the Absolute Characterization of Macromolecules. *Anal. Chim. Acta.* 272:1–40.
47. Friebe, P., and E. Harris. 2010. Interplay of RNA elements in the dengue virus 5' and 3' ends required for viral RNA replication. *J. Virol.* 84:6103–6118.
48. Deo, S., T. R. Patel, …, S. A. McKenna. 2015. Characterization of the termini of the West Nile virus genome and their interactions with the small isoform of the 2' 5'-oligoadenylate synthetase family. *J. Struct. Biol.* 190:236–249.
49. Li, D., H. T. Lu, …, Z. Y. Liu. 2023. Specialized cis-Acting RNA Elements Balance Genome Cyclization to Ensure Efficient Replication of Yellow Fever Virus. *J. Virol.* 97:e0194922.
50. de Borba, L., S. M. Villordo, …, A. V. Gamarnik. 2015. Overlapping local and long-range RNA-RNA interactions modulate dengue virus genome cyclization and replication. *J. Virol.* 89:3430–3437.

Please cite this article in press as: Robinson et al., Structural dynamics of dengue virus UTRs and their cyclization, Biophysical Journal (2025), https://doi.org/10.1016/j.bpj.2025.09.004

51. Aguilar, R., K. B. Spencer, …, J. T. Lee. 2022. Targeting Xist with compounds that disrupt RNA structure and X inactivation. *Nature.* 604:160–166.

52. Badmalia, M. D., H. Sette Pereira, …, T. R. Patel. 2022. A comprehensive review of methods to study lncRNA-protein interactions in solution. *Biochem. Soc. Trans.* 50:1415–1426.

53. Lipfert, J., V. B. Chu, …, E. Synchrotron. 2007. Low-resolution models for nucleic acids from small-angle X-ray scattering with applications to electrostatic modeling. *J. Appl. Crystallogr.* 40:229–234.

54. Lipfert, J., R. Das, …, S. Doniach. 2007. Structural transitions and thermodynamics of a glycine-dependent riboswitch from Vibrio cholerae. *J. Mol. Biol.* 365:1393–1406.

55. Choi, K. H., and M. Morais. 2014. Use of small-angle X-ray scattering to investigate the structure and function of dengue virus NS3 and NS5. *Methods Mol. Biol.* 1138:241–252.

56. Zheng, W., and R. B. Best. 2018. An Extended Guinier Analysis for Intrinsically Disordered Proteins. *J. Mol. Biol.* 430:2540–2553.

57. Jacques, D. A., and J. Trewhella. 2010. Small-angle scattering for structural biology–expanding the frontier while avoiding the pitfalls. *Protein Sci.* 19:642–657.

58. Putnam, C. D., M. Hammel, …, J. A. Tainer. 2007. X-ray solution scattering (SAXS) combined with crystallography and computation: defining accurate macromolecular structures, conformations and assemblies in solution. *Q. Rev. Biophys.* 40:191–285.

59. Cantara, W. A., E. D. Olson, and K. Musier-Forsyth. 2017. Analysis of RNA structure using small-angle X-ray scattering. *Methods.* 113:46–55.

60. Grant, T. D., J. R. Luft, …, E. H. Snell. 2015. The accurate assessment of small-angle X-ray scattering data. *Acta Crystallogr. D Biol. Crystallogr.* 71:45–56.

61. Tants, J. N., and A. Schlundt. 2023. Advances, Applications, and Perspectives in Small-Angle X-ray Scattering of RNA. *Chembiochem.* 24: e202300110.

62. Jones, C. P., W. A. Cantara, …, K. Musier-Forsyth. 2014. Small-angle X-ray scattering-derived structure of the HIV-1 5' UTR reveals 3D tRNA mimicry. *Proc. Natl. Acad. Sci. USA.* 111:3395–3400.

63. Sun, Y. T., and G. Varani. 2022. Structure of the dengue virus RNA promoter. *RNA.* 28:1210–1223.

64. Bujalowski, P. J., W. Bujalowski, and K. H. Choi. 2017. Interactions between the Dengue Virus Polymerase NS5 and Stem-Loop A. *J. Virol.* 91:e00047-17.

65. Afonine, P. V., B. P. Klaholz, …, A. Urzhumtsev. 2018. New tools for the analysis and validation of cryo-EM maps and atomic models. *Acta Crystallogr. D Struct. Biol.* 74:814–840.

66. Mishra, B., and R. Aduri. 2022. The RNA Secondary Structure Analysis Reveals Potential for Emergence of Pathogenic Flaviviruses. *Food Environ. Virol.* 14:10–29.

67. Petoukhov, M. V., D. Franke, …, D. I. Svergun. 2012. New developments in the ATSAS program package for small-angle scattering data analysis. *J. Appl. Crystallogr.* 45:342–350.

68. Villordo, S. M., J. M. Carballeda, …, A. V. Gamarnik. 2016. RNA Structure Duplications and Flavivirus Host Adaptation. *Trends Microbiol.* 24:270–283.

69. Zhang, Y., Y. Zhang, …, X. Fang. 2019. Long non-coding subgenomic flavivirus RNAs have extended 3D structures and are flexible in solution. *EMBO Rep.* 20:e47016.

70. de Borba, L., S. M. Villordo, …, A. V. Gamarnik. 2019. RNA Structure Duplication in the Dengue Virus 3' UTR: Redundancy or Host Specificity? *mBio.* 10:e02506-18.

71. Liu, H., J. Zhang, …, G. Liang. 2021. The 5' and 3' Untranslated Regions of the Japanese Encephalitis Virus (JEV): Molecular Genetics and Higher Order Structures. *Front. Microbiol.* 12:730045.

72. Chen, Y., and L. Pollack. 2016. SAXS studies of RNA: structures, dynamics, and interactions with partners. *Wiley Interdiscip. Rev. RNA.* 7:512–526.

73. Grant, T. D. 2018. Ab initio electron density determination directly from solution scattering data. *Nat. Methods.* 15:191–193.

74. Nomaguchi, M., M. Ackermann, …, R. Padmanabhan. 2003. De novo synthesis of negative-strand RNA by Dengue virus RNA-dependent RNA polymerase in vitro: nucleotide, primer, and template parameters. *J. Virol.* 77:8831–8842.

75. Klema, V. J., M. Ye, …, K. H. Choi. 2016. Dengue Virus Nonstructural Protein 5 (NS5) Assembles into a Dimer with a Unique Methyltransferase and Polymerase Interface. *PLoS Pathog.* 12:e1005451.

76. Liu, Z. Y., X. F. Li, …, C. F. Qin. 2016. Viral RNA switch mediates the dynamic control of flavivirus replicase recruitment by genome cyclization. *eLife.* 5:e17636.

77. Lee, E., P. J. Bujalowski, …, K. H. Choi. 2021. Structures of flavivirus RNA promoters suggest two binding modes with NS5 polymerase. *Nat. Commun.* 12:2530.

78. Kikhney, A. G., C. R. Borges, …, D. I. Svergun. 2020. SASBDB: Towards an automatically curated and validated repository for biological scattering data. *Protein Sci.* 29:66–75.